J Mater Sci (2024) 59:2302–2314

Chemical routes to materials

Deposition of Pd–Pt alloy zigzag shell over Au nanorods for boosted catalysis and thermo-photo catalysis

Yun-Qi Dou[1], Qi Zhang[1], Tian-Song Deng[1,*], Zhiqun Cheng[1], and Xiaoyu Zhao[2]

[1] *School of Electronics and Information Engineering, Hangzhou Dianzi University, Hangzhou 310018, People's Republic of China*
[2] *College of Materials and Environmental Engineering, Hangzhou Dianzi University, Hangzhou 310018, People's Republic of China*

Received: 15 June 2023
Accepted: 3 January 2024
Published online:
5 February 2024

ABSTRACT

Multimetallic plasmonic nanostructures, with appropriate morphology, elemental proportions and sizes, can be used to accelerate photocatalytic reactions. Here, we designed zigzag trimetallic nanostructures with the Au core and Pd–Pt alloy shell, whose catalytic ability was boosted by the synergistic effect of the plasmonic metal and catalytic metal. The catalytic rate of Au@PdPt nanoparticle (NP) with no light have a significant improvement, attributed to the larger contact area provided by the zigzag alloy shell. Furthermore, the enhanced catalytic activity in the presence of light is primarily due to the thermo-photo catalytic effect of plasmonic Au. The adding ratios of Pd:Pt were adjusted from 1:4 to 4:1, and we found that, when adding the Pd:Pt of 1:1, the zigzag Au@PdPt nanoparticle (NP) exhibited a superior reaction rate in the reduction methylene blue (MB) under light illumination. The rate is 8 times higher than that of Au@Pt, and the reduction conversion reached 100%. And it has a favorable plasmon enhancement factor with an appropriate shell thickness and get the balance between the catalytic performance and economic effects. This structure driven by capability-oriented design principles and holds the potential for applications in the field of catalysis.

Handling Editor: Pedro Camargo.

Address correspondence to E-mail: dengts@pku.edu.cn

https://doi.org/10.1007/s10853-024-09351-8

GRAPHICAL ABSTRACT

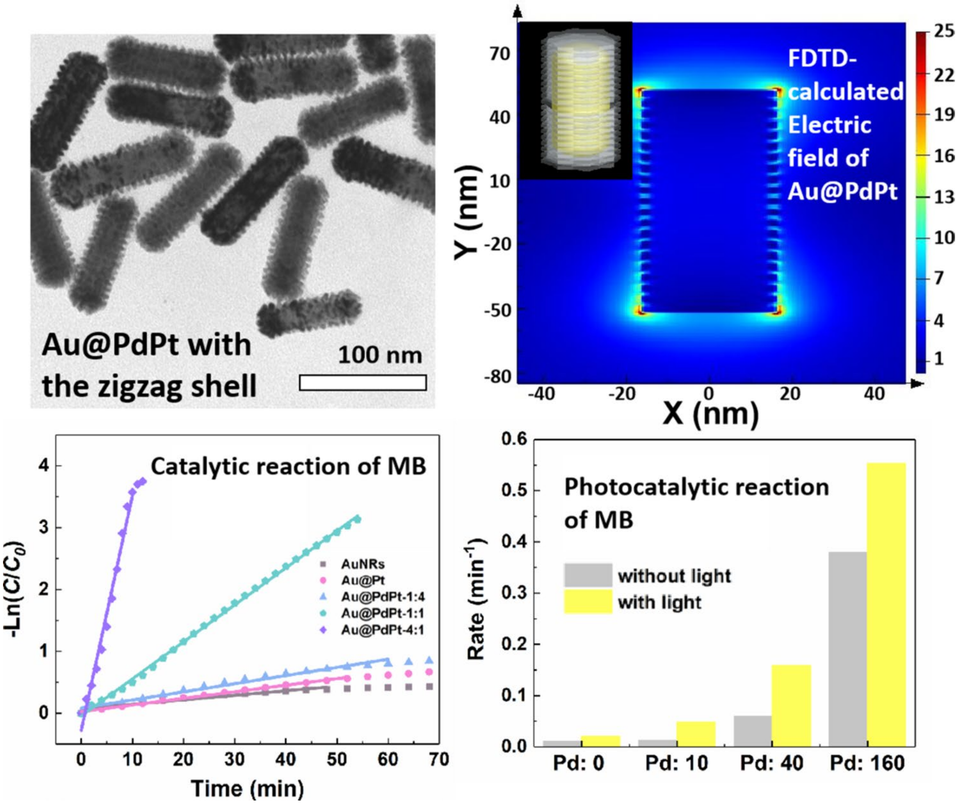

Introduction

Multimetallic plasmonic nanostructures, one of the hottest research topics recently, have intrigued numerous researchers to further explode [1–3]. Localized surface plasmon resonance (LSPR) is a coherent oscillation of the free carrier cloud in the metal triggered by the incoming light wave [4], which is potential for application of multicomponent structures. Multimetallic plasmonic nanostructures, emerging as the ability-oriented materials, could enhance the optical, electronic or catalytic performances by tuning their size, component or morphology [5–11]. This enhancement is beneficial to further advance their application in fields such as imaging [12, 13], therapy [14, 15], sensing [16–18] and catalysis [19–21].

Especially in the domain of catalysis [22–25], leading the plasmonic material into a multicomponent system can harness their LSPR effect to facilitate the photothermal conversion, the hot electron generation [26, 27]. In a complex catalytic system composed of plasmonic metals and other materials, the local high temperature induced by the electric field on the plasmonic mental surface can accelerate the catalytic reactions under mild conditions. Here, the synergetic effect of thermal and photo energies is usually greater than the individual thermal or photo catalysis [28]. Based on this superiority, the thermo-photo catalysts have garnered more and more attention and exploration. In Cai's work [29], the Au–Pd/TiO_2 was designed as a thermo-photo catalyst to drive the redox reactions. By exploring the role of different wavelengths of light, it was verified that the Au–Pd nanoparticles can absorb visible light and provide the local heat to promote the reaction. Au nanorods, having the LSPR effects aroused by the light in the visible and near infrared (NIR) regions [2] and accurately tuned by changing their aspect ratio (AR) [30], are the optimal choice for the multicomponent structures to fully harvest the broad-wavelength sunlight for thermo-photo catalysis [31–33]. For example, in Hu's work [34], the Au nanorods superlattice array were vertically ordered on the TiO_2 films to promote the photocatalytic hydrogen evolution rate. It is the LSPR, including local electromagnetic field effect excited by the visible light, that enhances photocatalytic performance of this film for H_2 evolution. Besides, the catalytic performance is further enhanced when combined with other materials, like Pd, Pt, which have different work functions that facilitate hot electron transfer and electron–hole pair generation [26, 35–37]. Wu's group [38] compounded the Ag nanocrystals onto the Au@Cu_2O core–shell nanospheres, which lessened the catalytic reduction time of methyl orange from 50 to 4 min, and improved their stability and reusability. Zhang et al. [39] obtained the Au@AgPt hollow alloy shell nanostructures by introducing Pt into the Au@Ag nanostructures, and the photocatalytic reduction reaction rate is ~ 3 times higher than bimetallic Au@Ag nanorods. As can be seen, the performance of catalytic nanostructures demonstrates a marked improvement as a result of the addition of a third material.

Therefore, in our work, we designed a trimetallic nanostructure by introducing Pd in Au@Pt to optimize its morphology and enhance its thermo-photo catalytic activity by the synergistic mechanism among different materials. We adjusted the proportion of added Pd/Pt to create a zigzag Pd–Pt alloy shell with an appropriate thickness, enlarging the catalytic contact area while maintaining the LSPR effects. By combining the catalytic reduction of methylene blue (MB) and electric field simulations of different Au@PdPt samples, we discovered that the Au@PdPt nanoparticles can efficiently promote the reaction rate of MB by thermo-photo catalytic effects. Notably, the Au@PdPt nanoparticles with a Pd:Pt ratio of 1:1 are the optimal catalysts offering a balance of good plasmonic efficiency, catalytic conversion and economic benefits for thermo-photo catalysis.

Results and discussion

The used Au nanorods (AuNRs), synthesized by the seed-mediated growth method, have the average length of 93 nm and width of 24 nm (Fig. S1a), giving a narrow LSPR peak at 802 nm (Fig. S1b), which can efficiently absorb visible light. The aimed Au@PdPt nanostructures were acquired by adding CTAB, K_2PtCl_4, Na_2PdCl_4 and ascorbic acid (AA) at 65 °C, orderly. When only the Pt^{2+} ions were added, lots of dendritic particles of Pt deposited disorderly on the surface of AuNRs (Fig. 1a). However, with a fixed amount of the Pt^{2+}, the extra addition of Pd^{2+} altered

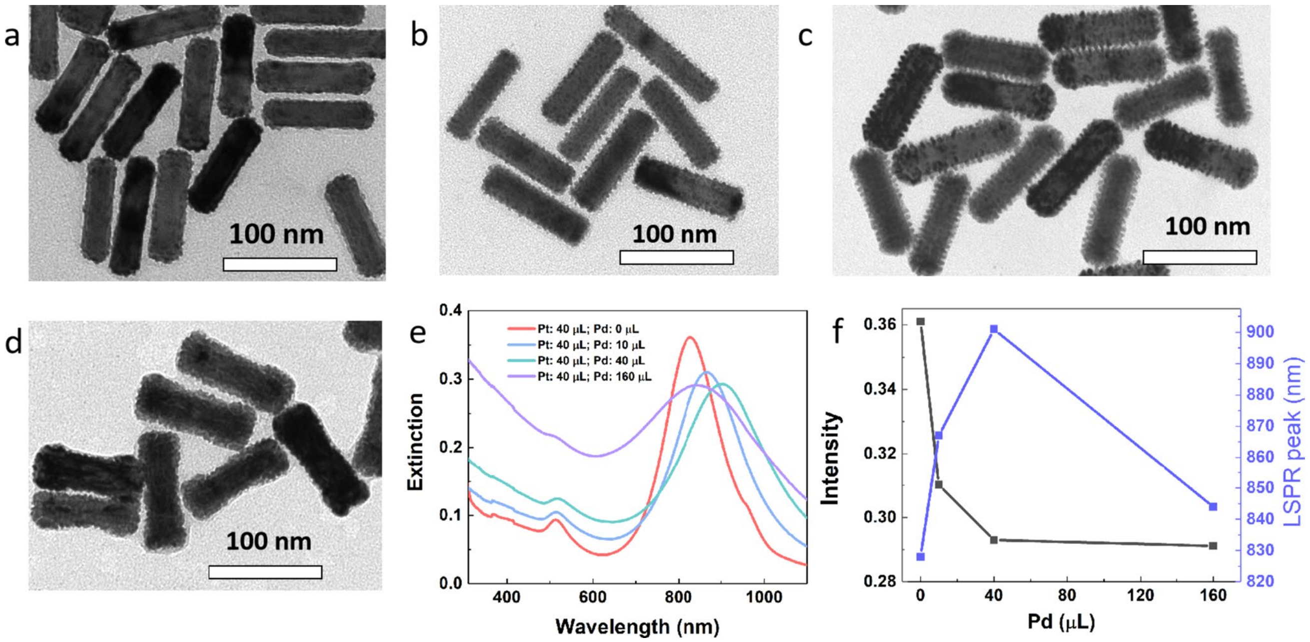

Figure 1 The morphology and spectra of Au@PdPt nanostructures with a fixed amount of the Pt^{2+} (40 μL) and different amounts of Pd^{2+}. TEM images of Au@PdPt synthesized by adding 0 μL (**a**), 10 μL (**b**), 40 μL (**c**) and 160 μL (**d**) of Pd^{2+}. **e** UV–vis-NIR extinction spectra of Au@Pt and three Au@PdPt samples. **f** Variation of the LSPR peaks and intensity as a function of the amount of Pd^{2+}.

the morphology of Au@Pd nanostructures. In the Fig. 1b, when 10 μL of Pd^{2+} was added simultaneously with the Pt precursor, small Pd–Pt alloy particles, ~ 1 nm in size, orderly formed on the AuNRs. As the volume of Pd^{2+} increased to 40 μL, the shells became thicker and the well-defined zigzag Pd–Pt alloyed shells were observed in the TEM image of Fig. 1c. These alloy island deposits were densely arranged and about 3 nm in size. Then, the Au@PdPt nanostructures with rough shells and larger tips were obtained due to the excessive Pd^{2+}, of 160 μL (Fig. 1d). The shells thickness at the body part is about 3 nm, while the shells thickness at both ends is about 5 nm. We got three samples of Au@PdPt NPs with different adding ratios of Pd:Pt, so we named them Au@PdPt-1:4, Au@PdPt-1:1 and Au@PdPt-4:1, respectively. Figure 1e shows the extinction spectra of Au@PdPt nanoparticles as the Pd–Pt ratio changes. According to these spectra, the trend of peak position and intensity as a function of Pd^{2+} volume are plotted in Fig. 1f. The LSPR peak red-shifted firstly, followed by a blue-shift, which is mainly determined by the morphology of composite nanoparticles based on AuNRs. At first, the introduction of a small quantity of Pd (< 160 μL) leads to the uniform distribution of Pd–Pt on the surface of AuNRs and a larger AR than Au@Pt, causing the peak position to red-shift. And then, the addition of excessive Pd (≥ 160 μL) leads to the wide tips and a reduction of AR, making the peak position blue-shift. At the same time, the intensity gradually became weaker. This is due to the large imaginary part of dielectric function of Pd and Pt, which leads to the plasmonic damping and hinders the LSPR effect of Au core [26].

To explore deposition mode of Pd and Pt with different molar ratio of added Pd/Pt, the Au@PdPt nanoparticles were characterized using the energy-dispersive X-ray spectroscopy (EDS) and high-resolution TEM (HRTEM). Figures 2a and S2 show the EDS mapping of Au (pink), Pd (blue) and Pt (green) of different Au@PdPt samples. By analyzing the element distribution within the square area of three Au@PdPt samples (Figs. 2b and S3), we founded that the Pt was always uniformly distributed on the AuNRs as island particles. Meanwhile, as increasing the amount of Pd^{2+}, the Pd gradually formed a thin shell covering the AuNRs. The thin Pd shell of Au@PdPt-1:1 was ~ 1 nm, and the shell thickness of Au@PdPt-4:1 increased to ~ 3 nm. The element distribution on the tip of Au@PdPt-4:1 was measured (Fig. S3c), reflecting that the core–shell structures formed when the added Pd^{2+} reached 160 μL and the massive deposition of Pd widened the ends of the Au@PdPt NPs, which further confirmed the blue-shift of spectra of Au@PdPt-4:1. The crystalline nature of the Au@PdPt NPs were analyzed by HRTEM images in Figs. 2c and S4. For the Au@PdPt-1:4 and Au@PdPt-1:1 NPs, the crystal plane spacing of Pd–Pt alloyed shells is 0.193 nm along the Au {200} facets (Fig. 2c), and the crystal plane spacing of Pd–Pt alloyed shells is 0.225 nm along the Au {111} facets (Fig. S4a), and they are similar to the Pt {200} and {111} facets, respectively. It reveals that the Pt lattices dominant the Pd–Pt alloy shells at the added Pd/Pt of 1:4 and 1:1. When the added Pd/Pt increased to 4:1, the Pd lattices dominant the Pd–Pt alloy shells, indicated by the fact that the crystal plane spacing of Pd–Pt alloyed shells is 0.189 nm along the Au {200} facets (Fig. S4b). And the fast Fourier transform (FFT) images of Au@PdPt-1:1 are exhibited in Fig. 2d. The diffraction pattern of zigzag Pd–Pt islands is same as the part of AuNRs, revealing the Pd–Pt shells are mainly constructed by {111} facets, {200} facets and the shells grow epitaxially. And the epitaxial growth occurred for all Au@PdPt samples with different amount of Pd because they have similarly lattice constants (Au: 4.08 Å; Pd: 3.89 Å; Pt: 3.92 Å) [40].

The X-ray photoelectron spectroscopy (XPS) spectra of Au@PdPt-1:1 was measured for surface element composition. The XPS spectra of Au (Fig. 2e) show the two peaks at 83.58 and 87.28 eV, which are Au^0 $4f_{7/2}$ and Au^0 $4f_{5/2}$, respectively. Figure 2f shows the peak of Pd^0 at 335.08 eV, 340.48 eV. And the peak of Pt^0 at 70.78 eV, 74.48 eV are showed in Fig. 2g. The peaks of Pd and Pt deviate slightly, compared with the standard values of commercial Pd/C ($3d_{5/2}$: 335.80 eV; $3d_{3/2}$: 340.80 eV) and commercial Pt/C ($4f_{7/2}$: 71.30 eV; $4f_{5/2}$: 74.30 eV) [10], which is possibly owing to the electronic interaction in Pd–Pt alloyed shell. The composition and the crystalline structure of Au@PdPt-1:1 were further explored by X-ray powder diffraction (XRD) (Fig. S5). The diffraction peaks at 38.3°, 44.3°, 64.8° and 77.4° are indexed to the (111), (200), (220) and (311) planes of face-centered-cubic (fcc) Au, respectively. Within the blue dashed boxes, there are the asymmetrical drops on the right sides, indicating that the very weak diffraction peaks assigned to the (111), (220) of fcc Pd were detected [41]. The peaks observed at 44.7°, 78.2° are attributed to the (220), (311) phase of PdPt alloy shell. There are the clear shifts in the two peaks, compared with the standard values (Pd: PDF#46-1043& Pt: PDF#04-0802), which may be from

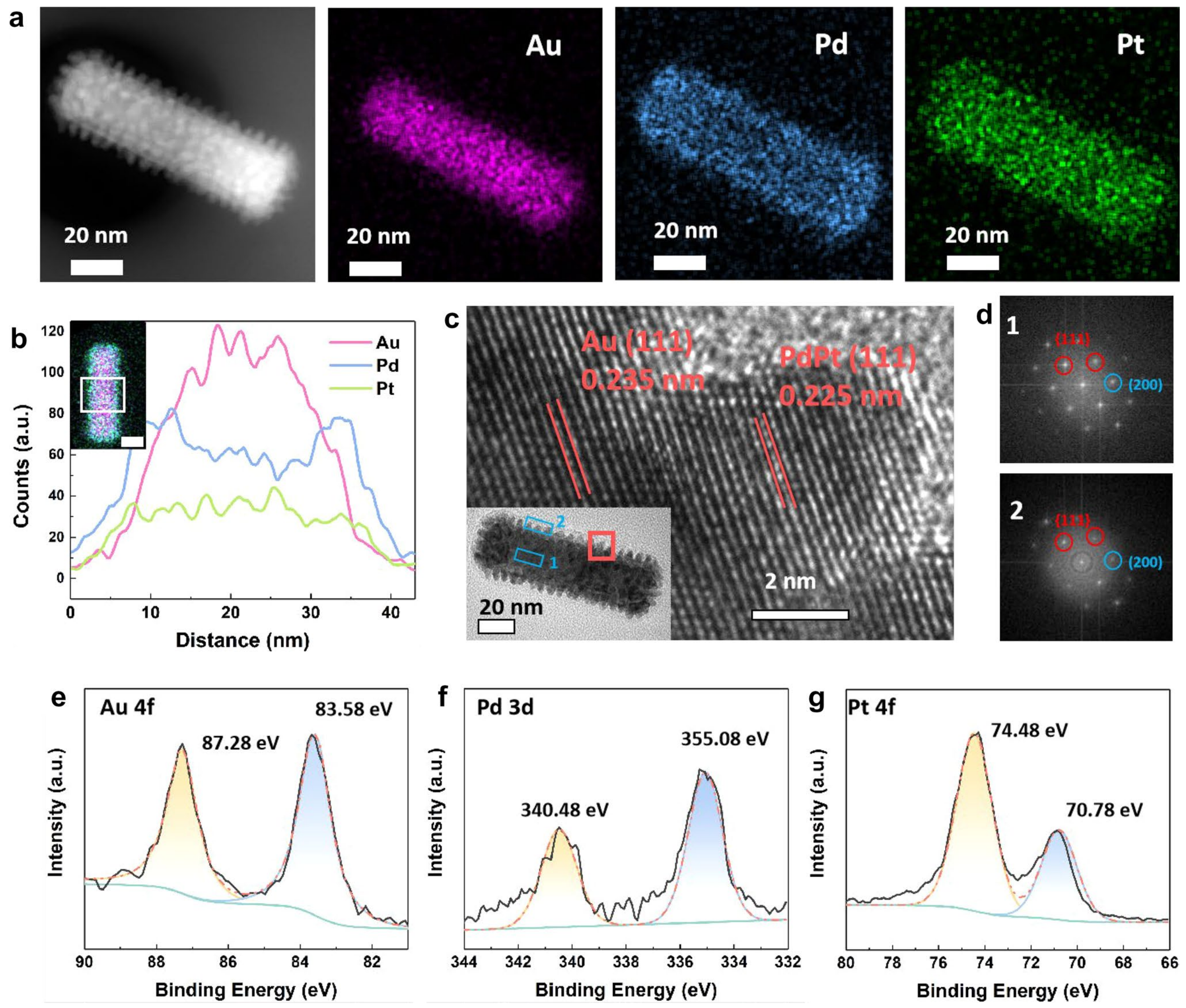

Figure 2 Characterization of Au@PdPt nanostructures. **a** The HAADF-STEM image and EDS elemental distribution of Au@PdPt NPs with 40 μL of Pd^{2+}. **b** The distribution of different elements in the white box of Au@PdPt-1:1 NPs in the upper left inset. The scales bar is 20 nm. **c** HRTEM images of interface between Au and zigzag Pd–Pt alloy shells. **d** Fast Fourier transform (FFT) of the blue squared regions 1&2 in (**c**). XPS spectra of Au@PdPt-1:1 NPs: **e** Au 4*f*, **f** Pd 3*d*, **g** Pt 4*f*.

the lattice strain at the interface between Au core and Pd–Pt shell [42].

For the formation of zigzag-like alloy shell, the surface energy (E_S) of Pt is greater than that of Au, and the bond dissociation energy (E_D) of Pt–Pt is greater than that of Au–Au, which means only the discontinuous, rough Pt shells grow on the AuNRs. However, the E_S of Pd is greater than that of Au, but the E_D of Pd–Pd is less than the E_D of Au–Au [43]. Therefore, it can be inferred that the added Pd plays the role of facilitating the transformation of Pt particles from disorder to order on the AuNRs. At the same time, the high temperature of 65 °C is another crucial factor for the formation of zigzag shell. In the work of Guo's group [44], the rough Pd–Pt alloy shell deposited on the AuNRs and the Au@PdPt core–shell nanoparticles were obtained at room temperature. But at 65 °C, the CTAB is easier to distribute uniformly on the surface of AuNRs as the soft template, and free Pt/Pd precursors in solution easily diffuse and get reduced onto the Au NR surfaces [27]. What's more, the high temperature can accelerate the reduction rate of Pd^{2+} and

Pt^{2+} into Pd and Pt metals, especially for the reduction of Pd^{2+}, which also led to the formation of the thin Pd layer when the Pd is excessive.

To investigate the catalytic activity enhancement resulting from the synergistic effect of Au@PdPt trimetallic nanostructures, we chose the reduction reaction of MB assisted by $NaBH_4$ as our model system. When the $NaBH_4$ was added into the MB solution, the MB was reduced to a reduced MB state (leucomethylene blue). The phenomenon that the color of solution changing from blue to colorless is obviously observed, which can be monitored by the decline of the intensity of the characteristic peak of MB (627 nm). The reduction process of MB in dark and illuminating by a Xe lamp ($\lambda > 420$ nm) is recorded in Figs. S6, S7,and 3a using all different catalytic samples, including no catalysis, AuNRs, Au@Pt NPs and three kinds of Au@PdPt NPs. One can see that the descent speed of the special peak intensity in the extinction spectra of MB had an obvious difference. The catalytic rate curve was fitted by -Ln(C/C_0)-t in Fig. 3b and c, where C_0 is the initial extinction intensity of MB at 627 nm and the C is real-time extinction intensity of MB. Compared to the AuNRs, the catalytic rates of Au@Pt improved 1.4-fold in dark and 1.2-fold in light, but they still remain low. However, without illumination, the catalytic rates of Au@PdPt NPs with the Pd–Pt ratios from 1:4, 1:1 to 4:1 showed an enhancement of ~ 1.2, 6 and 35 times, compared to the Au@Pt (Fig. 3b). Under light irradiation, the catalytic rates of Au@PdPt NPs made an enhancement of ~ 2, 8 and 26 times, respectively (Fig. 3c). Owing to the introduction of another catalytic material-Pd based on the same volume of Au@Pt NPs added, the larger size and the zigzag-like morphological modification maybe are crucial reasons accelerating the process of the catalytic reaction without light, which provide the larger contact areas for absorbing more ions onto the particles.

However, the continuous increase in catalytic rate does not imply that the thicker shells are better. Economic benefits and plasmonic efficiency should also be taken into account- LSPR effect can be easily blocked by the thick Pd–Pt shells, and Au, Pt and Pd are all costly. Therefore, we explored the influence of different Pd–Pt ratios on LSPR effects, which contributed to the further enhancement in thermo-photo catalysis based on catalysis. Namely, we changed the Pd–Pt ratios by adjusting the added volume of Pd precursor, keeping the Pt precursor unchanged. In Fig. 4a, the bar graph is the reaction rate of reducing MB with light or without light, using the different catalysts with the increasing Pd^{2+}. Furtherly, we calculated the plasmonic enhancement factor (plasmonic EF) [45], and the trend of the plasmonic EF was shown as line chart in Fig. 4b. The plasmonic EF is calculated by K_{light}/K_{dark}, where the K_{light} and K_{dark} represent the reaction rates of reducing MB in light and dark conditions. With the addition volume of Pd precursor from 0 to 160 μL, the plasmonic EF is 1.9, 3.6, 2.7 and 1.4, respectively. With the increasing of Pd^{2+}, the plasmonic EF firstly increases and then decreases. The Au@PdPt-1:4 exhibits the largest plasmonic EF, owing to the uncovered Pd–Pt decorations on the surface of AuNRs, while using the Pd precursors over 40 μL, the Pd coverage forming on the AuNRs weakens the light-absorb ability of plasmonic AuNRs. Additionally, the

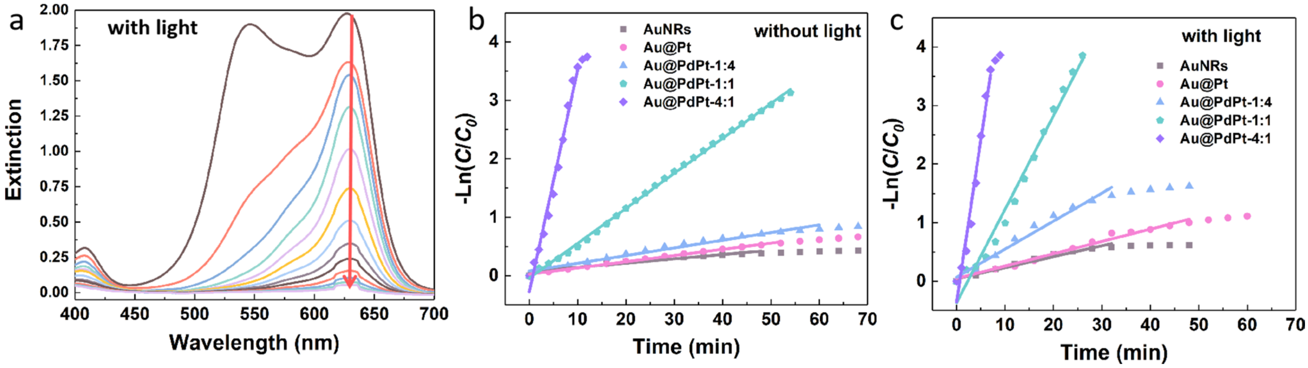

Figure 3 The comparison of catalytic ability between Au@PdPt NPs and other catalysts. **a** Time-dependent UV–vis extinction spectra of the reduction of MB assisted by $NaBH_4$ after adding Au@PdPt-1:1 in light irradiation, and measured every 2 min. Kinetic linear fitting curves for the reduction of MB with different kinds of catalysts without light (**b**) and under the light irradiation (**c**). The catalysts are AuNRs, Au@Pt NPs and Au@PdPt NPs with different Pd–Pt ratios.

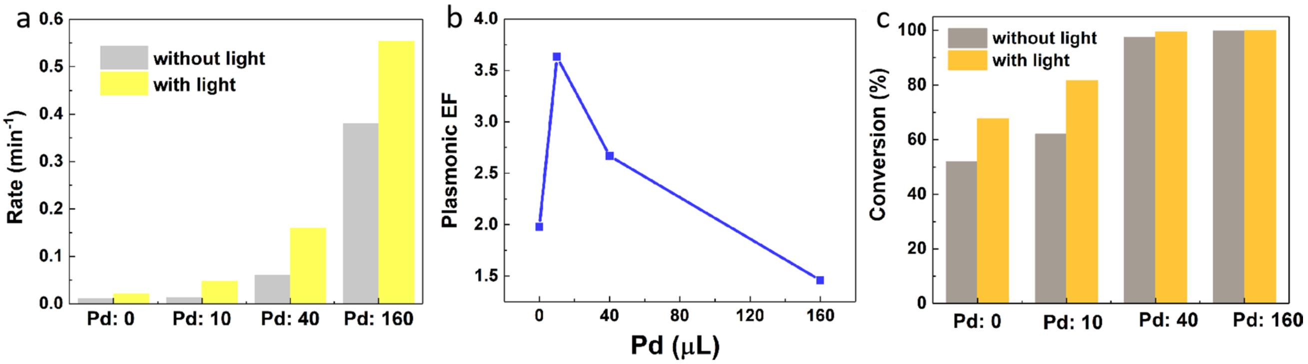

Figure 4 The catalytic characteristic of Au@PdPt NPs. **a** The reaction rate of reduction MB by Au@PdPt with the Pd^{2+} from 0 to 160 μL with and without light irradiation. The plasmonic enhancement factor (EF) (**b**) and the conversion (**c**) of Au@PdPt with different amount of Pd^{2+}.

dye conversion is a crucial measure for evaluating a catalyst, given that wastewater containing the MB with low concentrations is still harmful to the environment [46]. The conversion rate using catalysts with the different Pd^{2+} (from 0 to 160 μL) is 52%, 62%, 97%, 100% in dark and 68%, 82%, 100%, 100% in light, as shown in Fig. 4c. We found MB have a completely conversion only when the deposited catalytic metal reached a certain degree, like Au@PdPt-1:1 and Au@PdPt-4:1. Although the Au@PdPt-1:4 had the highest plasmonic EF, its conversion cannot get 100%. What's more, with the added Pd in Au@PdPt-4:1 being 4 times than that in Au@PdPt-1:1, the catalytic rate enhancement in the absence of light was more than 4 times, but the enhancement of catalytic rate in light did not quadruple. Therefore, considering both the plasmonic EF and conversion, the most suitable catalytic nanostructure for reducing MB is the Au@PdPt-4:1, while the most suitable thermo-photo catalyst for reducing MB is the Au@PdPt-1:1. Furthermore, the reusability is also an important property for the photocatalyst, which is worth for further investigation in our future work.

For the enhancement of reduction rate in the condition of light, the Au@PdPt NPs, acting as the thermo-photo catalyst [28], absorb the visible light and generate the local heat. And the work functions of Au, Pd, Pt are 5.10 eV, 5.12 eV and 5.65 eV, respectively, which also provides the possibility that the electron transfer between the three metals enhanced the catalytic rates by photoelectrocatalytic effect [26]. In the meanwhile, with the different Pd/Pt radio of Pd–Pt alloyed shell, the lattice strain [47] and some special chemical ordering [48] at the interface between Au core and Pd–Pt shell in different Au@PdPt samples also possibly lead to the different catalytic activities by affecting the energy level.

To investigate the relationship between LSPRs and the thermo-photo catalytic performance of the three Au@PdPt nanostructures, we calculated the spectra and electric field distribution of individual particle of Au@PdPt within each sample by using the finite-difference time domain (FDTD) simulations. Figure 5a shows the simulated spectra of Au@PdPt with different Pd/Pt ratio. Both the trends of peak intensity and the shifts of peak position are consistent with experimental data. Figure 5b–d shows the electric field distribution of ideal 3D models of the three Au@PdPt samples. The models were built according to the TEM images and given in the upper-right insets, and their elemental proportions were obtained from the EDS data. As seen, the electric-field enhancement mainly focuses on the surface of zigzag Pd–Pt alloy shells, and the strongest local electric fields are around the tips area, which means that the zigzag shells not only offer a bigger contact area, but also provide more hotspots from local electric-field enhancement. As the proportion of Pd increases, the electric field enhancement ability of Au@PdPt becomes weaker, resulting from the thicker Pd–Pt alloy shells and the disappearance of zigzag morphology. The results that the plasmonic EF dropped as the Pd^{2+} increased were well explained by the simulation. Therefore, appropriately adding some Pd to adjust the morphology of Pt shells deposited on the AuNRs is advantaged to optimize the thermo-photo catalytic performance of Au@PdPt.

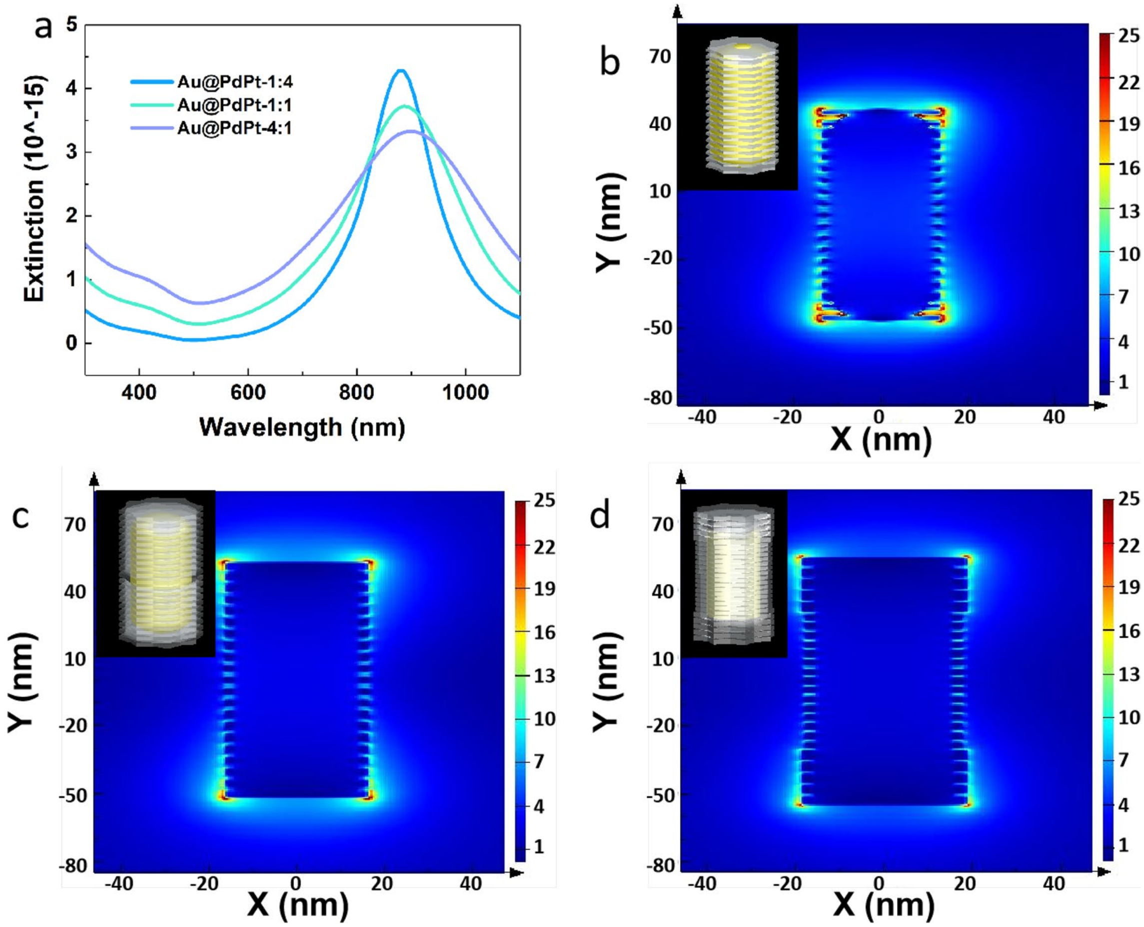

Figure 5 The FDTD simulations of Au@PdPt NPs. **a** The FDTD-calculated extinction spectra of Au@PdPt-1:4, Au@PdPt-1:1 and Au@PdPt-4:1. **b**–**d** Electric field distribution of the single Au@PdPt-1:4 (**b**), Au@PdPt-1:1 (**c**) and Au@PdPt-4:1 (**d**). The left-upper insets are the 3D model of Au@PdPt with different proportion of Pt and Pd.

Summary and conclusion

We synthesized new Au@PdPt trimetallic nanostructures by simultaneously adding Na_2PdCl_4 and K_2PtCl_4 solution at high temperature of 65 °C. The zigzag Pd–Pt alloy shell deposited on AuNRs were obtained by adjusting the Pd and Pt ratio. And combined with the EDS mapping and lining, the Pd and Pt were co-reduced and deposited evenly on the AuNRs when the Pd precursor is less than Pt precursor. However, a thin Pd layer formed firstly on the surface of AuNRs when the Pd precursor is more than Pt precursor, because the Pd precursors are easier to be reduced at the high temperature. And high temperature is helpful for the uniform distribution of CTAB and diffusion of Pd^{2+} and Pt^{2+}. Therefore, it is the introduction of Pd and a suitable temperature that led to a novel morphology of shell with regular arrangement like zigzag. A series of catalytic tests were conducted using the catalysts we synthesized, whether in dark or in light condition, the catalytic rate have an obvious improvement, which is were dominated by synergistic effect of LSPR of Au core and catalytic Pd–Pt shells. We simulated the local electric-field of different Au@PdPt, and founded that, as a composite catalytic system, it is essential to balance the catalytic promotion of Pd as a catalytic material with the barrier of Pd to the thermo-photo catalytic effect of plasmonic Au. Considering the synergistic effect and economic effects, the Au@PdPt-1:1 is the optimal catalyst, having a catalytic enhancement of 8 times than Au@Pt, with the plasmonic EF of 2.7, and 100% conversion under light conditions. We expect our work can pave the way for designing novel trimetallic nanostructures with synergistic effect and morphological control for thermo-photo catalysis.

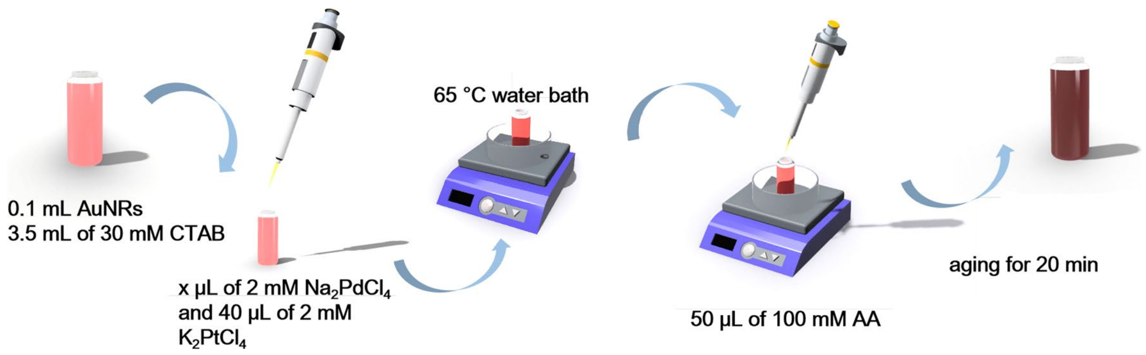

Scheme 1 Schematic illustration of the synthesis process.

Experimental

Chemicals

Hexadecyltrimethylammonium bromide (CTAB, > 99%) was purchased from TCI America. L-ascorbic acid (AA, > 99.99%), chloroauric acid ($HAuCl_4$), hydrochloric acid (HCl, 37 wt.% in water), sodium tetrachloropalladate(II) (Na_2PdCl_4), potassium tetrachloroplatinate(I) (K_2PtCl_4) and methylene blue (MB) were purchased from Shanghai Macklin Biochemical Technology Co., Ltd. Sodium borohydride ($NaBH_4$, 98%), sodium oleate (NaOL, > 99.8%) and silver nitrate ($AgNO_3$, > 99.8%) were purchased from Shanghai Aladdin Biochemical Technology Co., Ltd. Ultrapure water (Millipore Milli-Q grade) with a resistivity of 18.2 MΩ was used in all of the experiments. All chemicals were used as received without further purification.

Synthesis of AuNRs

The AuNRs were synthesized using a previously reported "seed-mediated method" [49] with slightly modification. For the seed solution, 0.25 mL of 10.0 mM $HAuCl_4$, 10 mL of 0.1 M CTAB and the freshly prepared ice-cold $NaBH_4$ (0.6 mL, 10.0 mM) were added into a 20 mL bottle. And the mixed solution was stirred and left it undisturbed for 30 min.

For the growth solution, 7.0 g of CTAB, 1.24 g NaOL and 250 mL of water were added in a 500 mL flask, magnetically stirring in 50 °C water bath. When the solution was cooled down to 30 °C, 24 mL of 4.0 mM $AgNO_3$ was added and kept it for 15 min. And then, 25 mL of 10.0 mM $HAuCl_4$ and 225 mL of water were added and the solution was magnetically stirred at 700 rpm for 1 h. The color of solution faded and 1.5 mL of HCl (37 wt.% in water) was added under the stirring at 700 rpm for 15 min. 1.25 mL of 64.0 mM AA and 0.4 mL of seed was injected into the mixture with stirring for 30 s. Finally, the resultant mixture were under static conditions at 30 °C overnight for AuNRs growth. The obtained AuNRs were acquired by centrifugation at 8000 rpm for 15 min, washed once with water and redispersed in 50 mL of 1.5 mM CTAB. For extinction spectra measurement, the AuNRs stock solution was diluted 35 times in the water, and the intensity of LSPR peak is 0.63 at 802 nm in a 1.0 cm cuvette.

Synthesis of Au@PdPt

The synthesis process was shown in Scheme 1. 0.1 mL of the prepared AuNRs were centrifuged to remove the supernatant and dispersed in 3.5 mL of 30 mM CTAB. Corresponding volume of 2 mM Na_2PdCl_4 and 40 μL of 2 mM K_2PtCl_4 were added and the solution was shaking to mix uniformly. 50 μL of 100 mM AA was added in 65 °C water bath and the mixture was aging for 20 min. The obtained Au@PdPt NPs were centrifuged at 8500 rpm for 15 min, washed once with water and redispersed in 0.35 mL of water for storage. The volume of Na_2PdCl_4 added to obtain three different Au@PdPt NPs samples are 10 μL, 40 μL and 160 μL, respectively.

Synthesis of Au@Pt NPs

0.1 mL of the prepared AuNRs were centrifuged to remove the supernatant and dispersed in 3.5 mL of 30 mM CTAB. 40 μL of 2 mM K_2PtCl_4 was added and the solution was shaking to mix uniformly. 50 μL of

100 mM AA was added in 65 °C water bath and the mixture was aging for 20 min. The obtained Au@Pt NPs were centrifuged at 8500 rpm for 15 min, washed once with water and redispersed in 0.35 mL of water for storage.

Thermo-photo catalytic/catalytic reduction of MB

In a cuvette, 1 mL of MB (0.1 mM) and 15 μL of catalyst were added, followed by the addition of a fresh-made $NaBH_4$ (100 μL, 25 mM) solution. After adding the catalysts, the solution gradually changed from blue to colorless. The spectra of MB, from 400 to 700 nm, were recorded at a regular interval.

For the thermo-photo catalytic reaction, we tested in the condition of "with light." we used a 250 W Xenon lamp (HDL-II, Suzhou Betical Optoelectronics Technology Co. Ltd., China) equipped with a filter in which the light wavelength less than 420 nm was cutoff.

For the catalytic reaction, we tested spectra with the lamp off in the dark room. And the other conditions are totally same with photocatalytic tests.

Characterization

The transmission electron microscope (TEM) images were obtained with a HT-7700 microscope (HITACHI, Japan) operated at 100 kV. Optical extinction spectra were recorded with a UV-1900i spectrophotometer (SHIMADZU, Japan). High-resolution TEM (HRTEM) images and energy disperse spectroscopy (EDS) mapping were performed by a Fei-Talos-F200S operated at 200 kV. The X-ray photoelectron spectroscopy (XPS) analysis was performed by Thermo Scientific K-Alpha. The XRD patterns of the samples were tested on Panalytical X'Pert3 Powder with Cu Kα radiation in the 2θ range from 25° to 90° at a scanning rate 2° min^{-1}. The particle sizes of the nanoparticles were measured from TEM images, whereby > 50 nanoparticles were measured for each sample.

FDTD calculations

The FDTD simulations of Au@PdPt nanostructures were carried out using a commercial software (Lumerical Solutions). The Au@PdPt nanostructures were modeled according to the TEM images and EDS elements distribution. The Au core was modeled using a rounded cylinder with a 12 nm of radius and 93 nm of z span. The shell of Au@PdPt-1:4 consisted of 19 Pd–Pt alloy star polygons, which has 8 points and 2 nm of z span. The shell of Au@PdPt-1:1 consisted of Pd Rounded cylinder shell with the thickness of 1 nm and 21 Pd–Pt alloy star polygons with 8 points and 3 nm of z span. The shell of Au@PdPt-4:1 consisted of Pd Rounded cylinder shell with the thickness of 3 nm, 15 Pd–Pt alloy star polygons with 8 points and 3 nm of z span and 10 Pd–Pt alloy star polygons with 8 points and 4 nm of z span. The 3 models are shown in the upper-left insets of Fig. 5.

All of the simulation boundaries were set as perfect matched layers (PMLs). The refractive index of the surrounding medium was taken to be 1.33—the refractive index of water. The total-field scattered-field source was used to realize the plane wave incidence and the wavelength was from 300 to 1100 nm. The mesh was set at 0.5 nm to calculate the electric filed distribution of Au@PdPt. The dielectric function of Au, Pd and Pt are all obtained from Palik [50]. The effective dielectric function of Pd–Pt alloy was calculated by Eq. (1), which was derived from the effective medium approximation (EMA) based on the Maxwell–Garnett equation [51]. The ε_{eff}, ε_{Pd} and ε_{Pt} are the dielectric function of Pd–Pt alloy, Pd and Pt, respectively. P is the proportion of Pt in Pd–Pt alloy, which was obtained from the EDS mapping. And the real and imaginary parts of ε_{eff} of Pd–Pt alloy are drawn in Fig. S8.

$$\varepsilon_{eff} = \varepsilon_{Pd}\frac{2\mathrm{P}(\varepsilon_{Pt} - \varepsilon_{Pd}) + \varepsilon_{Pt} + 2\varepsilon_{Pd}}{2\varepsilon_{Pd} + \varepsilon_{Pt} - \mathrm{P}(\varepsilon_{Pt} - \varepsilon_{Pd})} \tag{1}$$

Acknowledgements

The authors thank Sudan Shen for her assistance in TEM at State Key Laboratory of Chemical Engineering (Zhejiang University). T. S. Deng acknowledge financial support from Zhejiang Provincial Natural Science Foundation (Grant: LY24F050008), Zhejiang Provincial Educational Ministry Scientific Research Project (Grant: Y202352284), and National Natural Science Foundation of China (NSFC, Grant: 61905056). This work was also supported by National Key R&D Program of China (Grant: 2018YFE0207500), the National

Natural Science Foundation (Grant 91938201 and 61871169), Zhejiang Provincial Natural Science Foundation (Grant LZ20F010004) and Project of Ministry of Science and Technology (Grant D20011).

Author contributions

YQD analyzed investigation, writing—original draft and visualization. TSD prepared writing–review & editing, funding acquisition and supervision. QZ performed investigation. XYZ provided resources. ZQC approved funding acquisition.

Data availability

Not applicable.

Declarations

Conflict of interest The authors declare no conflict to interest in this work.

Ethical approval The authors declare that our work does not involve live subjects.

Supplementary Information The online version contains supplementary material available at https://doi.org/10.1007/s10853-024-09351-8.

References

[1] Sytwu K, Vadai M, Dionne JA (2019) Bimetallic nanostructures: combining plasmonic and catalytic metals for photocatalysis. Adv Phys X 4:1619480. https://doi.org/10.1080/23746149.2019.1619480

[2] Sayed M, Yu J, Liu G, Jaroniec M (2022) Non-noble plasmonic metal-based photocatalysts. Chem Rev 122:10484–10537. https://doi.org/10.1021/acs.chemrev.1c00473

[3] Baffou G, Quidant R, García de Abajo FJ (2010) Nanoscale control of optical heating in complex plasmonic systems. ACS Nano 4:709–716. https://doi.org/10.1021/nn901144d

[4] Ha M, Kim J-H, You M et al (2019) Multicomponent plasmonic nanoparticles: from heterostructured nanoparticles to colloidal composite nanostructures. Chem Rev 119:12208–12278. https://doi.org/10.1021/acs.chemrev.9b00234

[5] Zhang L, Jing H, Boisvert G et al (2012) Geometry control and optical tunability of metal-cuprous oxide core-shell nanoparticles. ACS Nano 6:3514–3527. https://doi.org/10.1021/nn300546w

[6] Kelly KL, Coronado E, Zhao LL, Schatz GC (2003) The optical properties of metal nanoparticles: the influence of size, shape, and dielectric environment. J Phys Chem B 107:668–677. https://doi.org/10.1021/jp026731y

[7] Grzelczak M, Pérez-Juste J, García de Abajo FJ, Liz-Marzán LM (2007) Optical properties of platinum-coated gold nanorods. J Phys Chem C 111:6183–6188. https://doi.org/10.1021/jp0671502

[8] Kim J, Hilal H, Haddadnezhad M et al (2022) Plasmonic all-frame-faceted octahedral nanoframes with eight engraved Y-shaped hot zones. ACS Nano 16:9214–9221. https://doi.org/10.1021/acsnano.2c01543

[9] Baffou G, Quidant R, Girard C (2009) Heat generation in plasmonic nanostructures: Influence of morphology. Appl Phys Lett 94:153109. https://doi.org/10.1063/1.3116645

[10] Liang W, Wang Y, Zhao L et al (2021) 3D anisotropic Au@Pt–Pd hemispherical nanostructures as efficient electrocatalysts for methanol, ethanol, and formic acid oxidation reaction. Adv Mater 33:2100713. https://doi.org/10.1002/adma.202100713

[11] Zhang R, Zheng P, Ma X (2017) Preparation and catalytic properties of magnetic rectorite-chitosan-Au composites. J Alloys Compd 690:381–389. https://doi.org/10.1016/j.jallcom.2016.08.131

[12] Liu X, Liu L, Hu X et al (2018) Multimodal bioimaging based on gold nanorod and carbon dot nanohybrids as a novel tool for atherosclerosis detection. Nano Res 11:1262–1273. https://doi.org/10.1007/s12274-017-1739-4

[13] Cheng K, Kothapalli S-R, Liu H et al (2014) Construction and validation of nano gold tripods for molecular imaging of living subjects. J Am Chem Soc 136:3560–3571. https://doi.org/10.1021/ja412001e

[14] Tang J, Jiang X, Wang L et al (2014) Au@Pt nanostructures: a novel photothermal conversion agent for cancer therapy. Nanoscale 6:3670–3678. https://doi.org/10.1039/c3nr06841b

[15] Ayala-Orozco C, Urban C, Knight MW et al (2014) Au Nanomatryoshkas as efficient near-infrared photothermal transducers for cancer treatment: benchmarking against nanoshells. ACS Nano 8:6372–6381. https://doi.org/10.1021/nn501871d

[16] Yuan Y, Yuan R, Chai Y et al (2010) A signal-on electrochemical probe-label-free aptasensor using gold–platinum

alloy and stearic acid as enhancers. Biosens Bioelectron 26:881–885. https://doi.org/10.1016/j.bios.2010.07.035

[17] Iglesias-Mayor A, Amor-Gutiérrez O, Novelli A et al (2020) Bifunctional Au@Pt/Au core@shell nanoparticles as novel electrocatalytic tags in immunosensing: application for alzheimer's disease biomarker detection. Anal Chem 92:7209–7217. https://doi.org/10.1021/acs.analchem.0c00760

[18] Chen J, Cheng G, Wu K et al (2020) Sensitive and specific detection of ractopamine: an electrochemiluminescence immunosensing strategy fabricated by trimetallic Au@Pd@Pt nanoparticles and triangular gold nanosheets. Electrochim Acta 361:137061. https://doi.org/10.1016/j.electacta.2020.137061

[19] Liu W, Zheng G, Wong W-L, Wong K-Y (2019) Au-Pd alloy nanoparticles catalyze the colorimetric detection of hydrazine with methylene blue. Inorg Chem Commun 107:107455. https://doi.org/10.1016/j.inoche.2019.107455

[20] Kondrat SA, Miedziak PJ, Douthwaite M et al (2014) Base-free oxidation of glycerol using titania-supported trimetallic Au-Pd-Pt nanoparticles. Chemsuschem 7:1326–1334. https://doi.org/10.1002/cssc.201300834

[21] Sun Y, Zhang W, Wang Q et al (2021) Biomass-derived N, S co-doped 3D multichannel carbon supported Au@Pd@Pt catalysts for oxygen reduction. Environ Res 202:111684. https://doi.org/10.1016/j.envres.2021.111684

[22] Ma L, Ding S-J, Yang D-J (2018) Preparation of bimetallic Au/Pt nanotriangles with tunable plasmonic properties and improved photocatalytic activity. Dalton Trans 47:16969–16976. https://doi.org/10.1039/C8DT03482F

[23] Lei W, Wang H, Zhang X et al (2022) Cu_2O-based binary and ternary photocatalysts for the degradation of organic dyes under visible light. Ceram Int 48:1757–1764. https://doi.org/10.1016/j.ceramint.2021.09.255

[24] Dutta SK, Mehetor SK, Pradhan N (2015) Metal semiconductor heterostructures for photocatalytic conversion of light energy. J Phys Chem Lett 6:936–944. https://doi.org/10.1021/acs.jpclett.5b00113

[25] Chen Y, Zhai Y, Deng L et al (2019) Optimizing Ag-Pt core-shell nanostructures for solar energy conversion, plasmonic photocatalysis, and photothermal catalysis. Appl Phys Lett 114:183902. https://doi.org/10.1063/1.5095669

[26] Yang H, He L-Q, Wang Z-H et al (2016) Surface plasmon resonance promoted photoelectrocatalyst by visible light from Au core Pd shell Pt cluster nanoparticles. Electrochim Acta 209:591–598. https://doi.org/10.1016/j.electacta.2016.05.120

[27] Guo J, Zhang Y, Shi L et al (2017) Boosting hot electrons in hetero-superstructures for plasmon-enhanced catalysis. J Am Chem Soc 139:17964–17972. https://doi.org/10.1021/jacs.7b08903

[28] Fang S, Hu YH (2022) Thermo-photo catalysis: a whole greater than the sum of its parts. Chem Soc Rev 51:3609–3647. https://doi.org/10.1039/D1CS00782C

[29] Cai X, Fang S, Hu YH (2021) Unprecedentedly high efficiency for photocatalytic conversion of methane to methanol over Au–Pd/TiO_2 – what is the role of each component in the system? J Mater Chem A 9:10796–10802. https://doi.org/10.1039/D1TA00420D

[30] González-Rubio G, Díaz-Núñez P, Rivera A et al (2017) Femtosecond laser reshaping yields gold nanorods with ultranarrow surface plasmon resonances. Science 358:640–644. https://doi.org/10.1126/science.aan8478

[31] Rong Y, Dandapat A, Huang Y et al (2016) Spatially-controlled growth of platinum on gold nanorods with tailoring plasmonic and catalytic properties. RSC Adv 6:10713–10718. https://doi.org/10.1039/C5RA23175B

[32] Wang F, Li C, Chen H et al (2013) Plasmonic harvesting of light energy for Suzuki coupling reactions. J Am Chem Soc 135:5588–5601. https://doi.org/10.1021/ja310501y

[33] Deng S, Zhang B, Choo P et al (2021) Plasmonic photoelectrocatalysis in copper-platinum core–shell nanoparticle lattices. Nano Lett 21:1523–1529. https://doi.org/10.1021/acs.nanolett.0c05029

[34] Hu L, Li Y, Peng X et al (2021) TiO_2 film supported by vertically aligned gold nanorod superlattice array for enhanced photocatalytic hydrogen evolution. Chem Eng J 417:127900. https://doi.org/10.1016/j.cej.2020.127900

[35] Wang L, Ge J, Wang A et al (2014) Designing p-type semiconductor-metal hybrid structures for improved photocatalysis. Angew Chem Int Ed 53:5107–5111. https://doi.org/10.1002/anie.201310635

[36] Sharma RK, Yadav S, Dutta S et al (2021) Silver nanomaterials: synthesis and (electro/photo) catalytic applications. Chem Soc Rev 50:11293–11380. https://doi.org/10.1039/D0CS00912A

[37] Xie C, Niu Z, Kim D et al (2020) Surface and interface control in nanoparticle catalysis. Chem Rev 120:1184–1249. https://doi.org/10.1021/acs.chemrev.9b00220

[38] Wu T, Kou Y, Zheng H et al (2020) A novel Au@Cu_2O-Ag ternary nanocomposite with highly efficient catalytic performance: towards rapid reduction of methyl orange under dark condition. Nanomaterials 10:48. https://doi.org/10.3390/nano10010048

[39] Zhang Q, Deng TS, Dou YQ et al (2022) Trimetallic nanostructures of silver-platinum alloy shells on gold nanorods for plasmon-mediated photocatalysis. ACS Appl Nano Mater 5:17048–17058. https://doi.org/10.1021/acsanm.2c03953

[40] Foiles SM, Baskes MI, Daw MS (1986) Embedded-atom-method functions for the fcc metals Cu, Ag, Au, Ni, Pd, Pt, and their alloys. Phys Rev B 33:7983–7991. https://doi.org/10.1103/PhysRevB.33.7983

[41] Zhang L, Zhang J, Kuang Q et al (2011) Cu^{2+}-assisted synthesis of hexoctahedral Au–Pd alloy nanocrystals with high-index facets. J Am Chem Soc 133:17114–17117. https://doi.org/10.1021/ja2063617

[42] Li X, Hong X (2016) PdPt@Au core@shell nanoparticles: alloyed-core manipulation of CO electrocatalytic oxidation properties. Catal Commun 83:70–73. https://doi.org/10.1016/j.catcom.2016.05.012

[43] van der Hoeven JES, Deng TS, van Blaaderen A (2021) Structural control over bimetallic core-shell nanorods for surface-enhanced Raman spectroscopy. ACS Omega 6:7034–7046. https://doi.org/10.1021/acsomega.0c06321

[44] Yang X, Wang Q, Qing S et al (2021) Modulating electronic structure of an Au-nanorod-core–PdPt-alloy-shell catalyst for efficient alcohol electro-oxidation. Adv Energy Mater 11:2100812. https://doi.org/10.1002/aenm.202100812

[45] Yong Z, Shi Q, Fu R, Cheng W (2021) Fine-tuning Au@Pd nanocrystals for maximum plasmon-enhanced catalysis. Adv Mater Interfaces 8:2001686. https://doi.org/10.1002/admi.202001686

[46] Konstantinou IK, Albanis TA (2004) TiO2-assisted photocatalytic degradation of azo dyes in aqueous solution: kinetic and mechanistic investigations. Appl Catal B Environ 49:1–14. https://doi.org/10.1016/j.apcatb.2003.11.010

[47] Geng X, Li S, Heo J et al (2022) Grain-boundary-rich noble metal nanoparticle assemblies: synthesis, characterization, and reactivity. Adv Funct Mater 32:2204169. https://doi.org/10.1002/adfm.202204169

[48] Kozlov SM, Kovács G, Ferrando R, Neyman KM (2015) How to determine accurate chemical ordering in several nanometer large bimetallic crystallites from electronic structure calculations. Chem Sci 6:3868–3880. https://doi.org/10.1039/C4SC03321C

[49] Ye X, Zheng C, Chen J et al (2013) Using binary surfactant mixtures to simultaneously improve the dimensional tunability and monodispersity in the seeded growth of gold nanorods. Nano Lett 13:765–771. https://doi.org/10.1021/nl304478h

[50] Palik ED, Ghosh G (1991) Part II, CRITIQUES, Subpart 1 Metals. Handbook of optical constants of solids. Academic Press, San Diego

[51] Maxwell-Garnett JC (1904) XII. Colours in metal glasses and in metallic films. Philos Trans R Soc Lond Ser Contain Pap Math Phys Character 203:385–420. https://doi.org/10.1098/rsta.1904.0024